Simulation of Atmospheric Boundary Layer Processes Using Local- and Nonlocal-Closure Schemes

KIRAN ALAPATY

Environmental Programs, MCNC-North Carolina Supercomputing Center, Research Triangle Park, North Carolina

JONATHAN E. PLEIM*

Air Resources Laboratory, National Oceanic and Atmospheric Administration, Research Triangle Park, North Carolina

SETHU RAMAN AND DEVDUTTA S. NIYOGI

Department of Marine, Earth and Atmospheric Sciences, North Carolina State University, Raleigh, North Carolina

DAEWON W. BYUN*

Air Resources Laboratory, National Oceanic and Atmospheric Administration, Research Triangle Park, North Carolina

ABSTRACT

A soil–vegetation–atmospheric boundary layer model was developed to study the performance of two local-closure and two nonlocal-closure boundary layer mixing schemes for use in meteorological and air quality simulation models. Full interaction between the surface and atmosphere is achieved by representing surface characteristics and associated processes using a prognostic soil–vegetation scheme and atmospheric boundary layer schemes. There are 30 layers in the lowest 3 km of the model with a high resolution near the surface. The four boundary layer schemes are tested by simulating atmospheric boundary layer structures over densely and sparsely vegetated regions using the observational data from the First ISLSCP (International Satellite Land Surface Climatology Project) Field Experiment (FIFE) and from Wangara.

Simulation results indicate that the near-surface turbulent fluxes predicted by the four boundary layer schemes differ from each other, even though the formulation used to represent the surface-layer processes is the same. These differences arise from the differing ways of representing subgrid-scale vertical mixing processes. Results also indicate that the vertical profiles of predicted parameters (i.e., temperature, mixing ratio, and horizontal winds) from the four mixed-layer schemes differ from each other, particularly during the daytime growth of the mixed layer. During the evening hours, after the mixed layer has reached its maximum depth, the differences among these respective predicted variables are found to be insignificant.

There were some general features that were associated with each of the schemes in all of the simulations. Compared with observations, in all of the cases the simulated maximum depths of the boundary layer for each scheme were consistently either lower or higher, superadiabatic lapse rates were consistently either stronger or weaker, and the intensity of the vertical mixing was either stronger or weaker. Also, throughout the simulation period in all case studies, most of the differences in the predicted parameters are present in the surface layer and near the top of the mixed layer.

1. Introduction

In regional meteorological modeling, the performances of physical parameterization schemes of varying complexity are usually intercompared by simulating a weather system driven by a strong mesoscale or synoptic-scale forcing. For example, Mahfouf et al. (1987) tested different atmospheric boundary layer (ABL) schemes in simulating mesoscale circulations initiated by surface contrasts. Stull and Driedonks (1987) showed that modeled mesoscale circulations and rainfall are sensitive to the representation of subgrid-scale vertical mixing processes. However, simulation of weakly forced synoptic circulations such as those that typically exist during the summer months over the United States is of lesser interest to meteorological modelers, because of the limited weather activity during these periods.

* Current affiliation: National Exposure Research Laboratory, U.S. Environmental Protection Agency.

Corresponding author address: Dr. Kiran Alapaty, Environmental Programs, MCNC-North Carolina Supercomputing Center, P.O. Box 12889, 3021 Cornwallis Road, Research Triangle Park, NC 27709-2889.
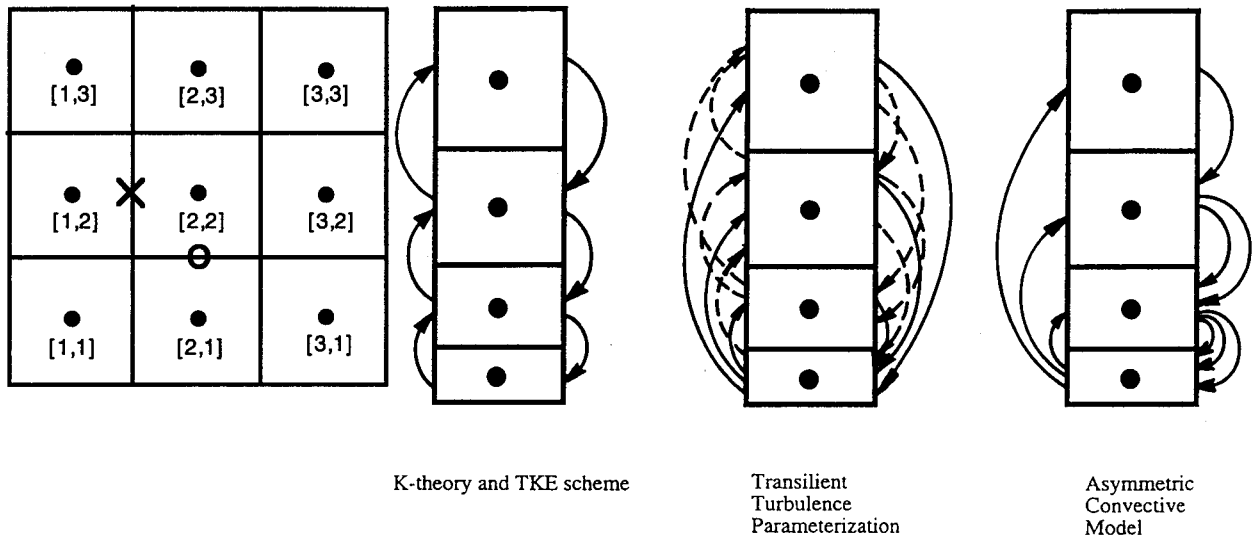E-mail: alapaty@flyer.ncsc.org

FIG. 1. (a) Simulation domain and grid structure used in the model. Closed circles represent center of grid cells. Arakawa C grid is used to predict u wind (eastward wind) at the location of the cross and v wind (northward wind) at the location of the open circle. (b) Schematic of mixing of air among grid cells due to turbulent eddies.

To air pollution modelers, on the other hand, accurate simulation of these types of circulation patterns is very important. Degradation of air quality due to released and chemically transformed pollutants is very common during the summer months over the eastern and western United States. Also, convective boundary layers are present during the daytime in the summer months. In the absence of cumulus convection, these pollutants are trapped in the ABL, further deteriorating air quality. Thus, accurate specification of weakly forced synoptic circulations and of the depth of the ABL as well as realistic representations of turbulent mixing processes are very important for air quality simulation studies. Higher-order-closure boundary layer schemes (Sun and Hsu 1988; Gao and Wesely 1994) are computationally expensive, particularly for use in air quality simulation models because one must solve several equations to predict the turbulent chemical fluxes of several chemical species. Thus, given the computational speed of present and near-future vector machines, it is impractical to use these schemes for operational purposes in meteorological and air quality modeling studies. As an alternative, many research and operational models use lower-order local- and nonlocal-closure boundary layer schemes.

In this paper, our overall objective is to study the performance of computationally viable two local-closure and two nonlocal-closure mixed-layer schemes in simulating ABL processes, within the context of a one-dimensional model. Note that because a three-dimensional model is required to evaluate these schemes, a relative preference for one scheme over another will not be established. The above objective has three parts: to test each scheme's functionality, to analyze each one's representativeness, and to explore each one's characteristic features in simulating the observed structures of

the ABL over distinct geographical regions. For this study and other follow-on studies to be presented later, we have developed a modular, one-dimensional soil–vegetation–boundary layer model for initial testing and implementation of different mixed-layer schemes into meteorological and air pollution models. Our next study with this model will use a chemical reaction formulation to study the effects of these vertical mixing schemes on tropospheric chemical concentrations. Finally, we will move to similar studies with three-dimensional meteorological and air pollution models.

2. The model

We developed a three-dimensional windowed model to study the effects of different representations of subgrid-scale vertical mixing on predicted boundary layer parameters using two local-closure and two nonlocal-closure mixed-layer schemes. The windowed model has 35 vertical sigma layers and 3 × 3 grid cells (Fig. 1a) in the horizontal. Essentially, this model is a one-dimensional soil–vegetation–boundary layer model in which predictions are made only at the central grid cell [2,2] for all vertical layers. This model can be used in two different ways. With the first option, the remaining eight horizontal grid cells (strictly, only the four grid cells [1,2], [2,1], [3,2], and [2,3]) in each layer provide lateral boundary conditions obtained from observations to the computational grid cell [2,2]. This option is the better choice when the effects of advection can be included in the model simulations. The second option can be used when observational data are available for only a single station. In this case, the eight horizontal grid cells surrounding the computational grid cell in each layer assume the same meteorological characteristics as

those of the computational grid cell. Thus, the model domain (nine grid cells) in each layer becomes horizontally homogenous, so advection terms have no effect on the model calculations.

Modular models like this one offer several advantages: they can be used efficiently for one-dimensional simulation and diagnostic studies, they can be used on any computer system, and they can easily be implemented into any two- or three-dimensional model without major modifications. In our study, we use the second option (i.e., a horizontally homogenous domain) to study the performance of four mixed-layer schemes. The governing equations and the parameterization schemes used are described below.

a. The governing equations

The general form of the dynamic and thermodynamic equations used in the model are

$$\frac{\partial u}{\partial t} = -u\frac{\partial u}{\partial x} - v\frac{\partial u}{\partial y} - \frac{\partial}{\partial z}(\overline{u'w'}) - f(v_g - v) \quad (1)$$

$$\frac{\partial v}{\partial t} = -u\frac{\partial v}{\partial x} - v\frac{\partial v}{\partial y} - \frac{\partial}{\partial z}(\overline{v'w'}) + f(u_g - u) \quad (2)$$

$$\frac{\partial T}{\partial t} = -u\frac{\partial T}{\partial x} - v\frac{\partial T}{\partial y} - \frac{\partial}{\partial z}(\overline{w'T'}) \quad (3)$$

$$\frac{\partial q_v}{\partial t} = -u\frac{\partial q_v}{\partial x} - v\frac{\partial q_v}{\partial y} - \frac{\partial}{\partial z}(\overline{w'q_v'}), \quad (4)$$

where u and v are the eastward and northward components of the wind, respectively; z is the altitude; the quantities in the parentheses are turbulent fluxes; f is the Coriolis parameter; T is temperature; q_v is the mixing ratio of water vapor; and u_g and v_g are the eastward and northward geostrophic winds, respectively.

b. The soil–vegetation model

Accurate representation of surface characteristics is very important because these control surface processes that affect the surface energy budget and hence the ABL processes. The soil–vegetation parameterization scheme used in this model is suggested by Noilhan and Planton (1989) and Jacquemin and Noilhan (1990). There are two soil layers, representing surface and subsurface processes; the first layer is 0.01 m thick and the second is 1 m thick. Prognostic equations to calculate the temperatures and soil moisture contents of these two layers are shown in Eqs. (5)–(8). The rate of change of the mean temperature of layer 1 can be written as

$$\frac{\partial T_{g1}}{\partial t} = C_T(R_n - S_{hf} - L_{hf}) - \frac{2\pi}{\tau}(T_{g1} - T_{g2}), \quad (5)$$

where T_{g1} and T_{g2} are the temperatures of layers 1 and 2, C_T is the inverse of thermal capacity of a particular type of soil, R_n is the net radiation at the surface, S_{hf}

and L_{hf} are the surface sensible and latent heat fluxes, and τ is the number of seconds in a day. The mean temperature of layer 2 is given by (Blackadar 1976):

$$\frac{\partial T_{g2}}{\partial t} = \frac{1}{\tau}(T_{g1} - T_{g2}). \quad (6)$$

Prognostic equations for the soil moisture for the two layers are given as

$$\frac{\partial W_{g1}}{\partial t} = \frac{C_1}{\rho_w d_1}(P_g - E_g) - \frac{C_2}{\tau}(W_{g1} - W_{geq}) \quad (7)$$

$$\frac{\partial W_{g2}}{\partial t} = \frac{1}{\rho_w d_2}(P_g - E_g - E_{tr}), \quad (8)$$

where W_{g1} and W_{g2} are the volumetric soil moisture contents for the two soil layers, ρ_w is the density of liquid water, d_1 and d_2 are the thicknesses of the two soil layers, P_g is the flux of liquid water reaching the soil surface, E_g is the evaporation at the soil surface, W_{geq} is the layer 1 soil moisture when gravity balances the capillary forces, and E_{tr} is the transpiration rate. For further details, refer to Noilhan and Planton (1989) and Jacquemin and Noilhan (1990).

The water content on the wet parts of the canopy due to rainfall and/or dew formation on the foliage is represented by W_r. The prognostic equation for W_r is based on Deardorff's (1978) formulation and can be written as

$$\frac{\partial W_r}{\partial t} = (V_c P_r) - E_r, \quad (9)$$

where V_c is the vegetation cover in fractional units, P_r is the precipitation rate at the top of the vegetation, and E_r is the evaporation rate from the wet parts of the canopy.

c. The radiation model

A simple radiation model is used in this study. Net radiation at the surface is calculated as the sum of incoming solar radiation absorbed at the surface, atmospheric longwave backscattering radiation, and outgoing longwave surface radiation. Solar radiation reaching the surface is a function of solar zenith angle, surface albedo, and atmospheric turbidity. Surface albedo is computed as the sum of minimum albedo with a solar zenith angle of zero and albedo changes due to the variation in the solar zenith angle (Idso et al. 1975; Pleim and Xiu 1995). Upward and downward longwave radiation are calculated as suggested by Anthes et al. (1987), which are functions of soil emissivity, ground temperature, atmospheric longwave emissivity, precipitable water in the atmosphere, and atmospheric temperatures.

d. Surface-layer formulation

The lower boundary layer (surface layer) is parameterized based on similarity theory suggested by Mon-

in and Yaglom (1971) using the nondimensional stability parameters Φ_m, Φ_h, and Φ_q for momentum, heat, and moisture, respectively. Turbulent sensible heat fluxes are computed using the relation given by

$$S_{hf} = u_* \theta_*,$$

where u_* is friction velocity and θ_* is the scale for temperature. Latent heat fluxes are computed from the soil-vegetation model discussed above, where bare-ground evaporation and evaporation from transpiring canopies and the wet parts of the canopies (due to dew formation and/or rainfall interception) are estimated. Thus, the total latent heat fluxes at the surface can be written as

$$L_{hf} = E_g + E_{tr} + E_r.$$

e. Boundary layer schemes

In our study, we used the two local-closure and two nonlocal-closure mixed-layer schemes described below—a K-theory-based scheme (local), a scheme based on turbulent kinetic energy and its dissipation rate (local), the transilient turbulence parameterization (nonlocal), and the asymmetric convective model (nonlocal). Figure 1b shows a schematic of eddies that can mix air among grid cells in a vertical column of air. In the local-closure schemes, K theory (BKT) and turbulent kinetic energy (TKE), vertical mixing is confined to adjacent grid cells. In the transilient turbulence parameterization (TTP) scheme, vertical mixing is determined by nonlocal mixing potentials such that mass can be transferred from any layer directly to any other layer in the entire model column. In the asymmetric convective model (ACM), a uniform amount of mass is distributed upward to all other grid cells in the ABL from the lowest grid cell. Downward transport goes from each grid cell to the adjacent lower grid cell. Thus, in the ACM upward mixing is nonlocal while the downward mixing is local.

1) K-THEORY-BASED SCHEME (BKT)

There are several K-theory-based schemes using different similarity theories. Since these are somewhat similar formulations, we consider the formulations suggested by Businger et al. (1971) and Hass et al. (1991) to represent the turbulent processes in the surface layer and mixed layer. Previous studies (Chang et al. 1987; Hass et al. 1991) have indicated that this type of formulation can provide better representation of turbulent mixing processes than other K-theory schemes. The coefficient of vertical eddy diffusivity, K_z, for the surface layer is

$$K_z = \frac{ku_* z}{\Phi_h(z/L)} \quad (10)$$

for the stable or neutral mixed layer; it is

$$K_z = \frac{ku_* z(1 - z/h)^2}{\Phi_h(z/L)} \quad \text{for } \frac{h}{L} \geq -10; \quad (11)$$

and for the unstable mixed layer, it is

$$K_z = kw_* z\left(1 - \frac{z}{h}\right) \quad \text{for } \frac{h}{L} < -10, \quad (12)$$

where k is the von Kármán constant, u_* is the friction velocity, h is the depth of the boundary layer, Φ_h is the nondimensional temperature profile, and w_* is the convective velocity. Note that the formulation for an unstable mixed layer (usually for daytime convective conditions) is very sensitive to the specification of the depth of the boundary layer, normally a poorly estimated variable. In the free atmosphere, turbulent mixing is parameterized using the formulation suggested by Blackadar (1979) in which vertical eddy diffusivities are functions of the Richardson number and wind shear in the vertical. This formulation can be written as

$$K_z = K_o + S(k\iota)^2 \frac{\text{Rc} - \text{Ri}}{\text{Rc}}, \quad (13)$$

where K_o is the background value (1 m^2 s^{-1}), S is the vertical wind shear, ι is the characteristic turbulent length scale (100 m), Rc is the critical Richardson number, and Ri is the Richardson number

$$\text{Ri} = \frac{g}{\Theta_v S^2} \frac{\partial \Theta_v}{\partial z},$$

where g is the acceleration due to gravity and Θ_v is virtual potential temperature.

2) TURBULENT KINETIC ENERGY SCHEME (TKE)

The prognostic equations used in this scheme to explicitly calculate the turbulent kinetic energy E and its dissipation rate ϵ are those suggested by Mellor and Yamada (1974). This scheme is often called a one-and-a-half-order closure scheme in which the unknown terms in the prognostic equations are parameterized in terms of local gradients of dynamic and thermodynamic parameters. The coefficient of vertical eddy diffusivity is calculated from the ratio of E and ϵ. Surface-layer similarity profiles (Businger et al. 1971) are used for obtaining boundary conditions for the prognostic equations for E and ϵ, while for the mixed layer the $E-\epsilon$ scheme is used. For further details, the reader is referred to Alapaty et al. (1994). In our study, we performed the model simulations using the second option described at the beginning of section 2 (i.e., the simulation domain is horizontally homogenous in each vertical layer). Thus, the advection terms in the governing equations (not shown) of E and ϵ have no effect on the model simulations. Therefore, these tests neglect the three-dimensional aspects of the TKE scheme (horizontal advection of E and ϵ), which are unique among these

schemes. The coefficients of eddy diffusivity for momentum and heat can be written as

$$K_m = \frac{c_2 E^2}{\epsilon}$$

$$K_h = K_m \frac{\Phi_m(z/L)}{\Phi_h(z/L)}, \qquad (14)$$

where c_2 is an empirical constant (Detering and Etling 1985) and Φ_m and Φ_h are nondimensional functions for momentum and heat (Businger et al. 1971).

3) TRANSILIENT TURBULENCE PARAMETERIZATION (TTP)

Turbulent eddies that exist in the ABL can transport heat, mass, and momentum over large vertical distances, often comparable to the depth of the ABL. Thus, at least during convective conditions, turbulent vertical mixing processes can be nonlocal. Stull and Driedonks (1987) use "transilient" (from the Latin for "jump over") to indicate nonlocal vertical mixing in their parameterization of the ABL. Let S be any variable such as potential temperature, horizontal wind components, mixing ratio, or the concentration of a trace gas species in the atmosphere. The new value of S due to subgrid-scale turbulent vertical mixing for a grid cell i at a future time $(t + \Delta t)$ can be written as

$$S_i(t + \Delta t) = \sum_{j=1}^{N} C_{ij}(t, \Delta t) S_j(t), \qquad (15)$$

where C is called the transilient matrix and i and j refer to two different grid cells in a column of atmosphere. In the turbulent mixing between grid cells i and j, C_{ij} represents the fraction of air mass ending in grid cell i that came from grid cell j, grid cell i is considered the "destination" cell, and grid cell j is considered the "source" cell. Thus, the change in the variable S due to subgrid-scale vertical mixing for grid cell i after a time interval Δt is a simple matrix multiplication with the value of S in the source cell. Estimation of the transilient matrix is the closure problem in this parameterization. This can be solved by considering the turbulent kinetic energy equation in nonlocal form. After parameterizing the unknown terms using the horizontal wind and temperature parameters, mixing potentials (Y) are obtained. Then, the transilient matrix C_{ij} can be written as

$$C_{ij} = \frac{m_j Y_{ij}}{\|Y\|_\infty} \quad \text{for } i \neq j,$$

where m_j is the mass of air in cell j, and $\|Y\|_\infty$ is called L_∞ norm of matrix Y. The diagonal elements (for $i = j$) of the transilient matrix can be written as

$$C_{ii} = 1 - \sum_{\substack{j=1 \\ i \neq j}}^{N} C_{ij}.$$

4) ASYMMETRIC CONVECTIVE MODEL (ACM)

The prognostic equation for the asymmetric convective model is the same as that of any other nonlocal closure scheme. However, the ACM differs from the TTP in that the transilient matrix is greatly simplified for greater computational efficiency and in the methodology used to compute fractional mass mixing rates. The ACM is based on Blackadar's nonlocal closure scheme (Blackadar 1979), which is based on the assumption that the turbulent mixing is isotropic (i.e., symmetric) in the ABL. Noting that the observational evidence and large-eddy simulation modeling studies of the mixing processes in a convective boundary layer are essentially asymmetric (i.e., turbulence is anisotropic) (Schumann 1989), Pleim and Chang (1992) modified this model by adding asymmetry in the vertical mixing processes. However, the ACM can be used only during convective conditions in the ABL. For other stability regimes, we use the BKT scheme described above to represent the ABL processes. Turbulent mixing in the ABL for any dynamic or thermodynamic variable can be written as

$$\frac{\partial S_i}{\partial t} = \sum_{j=1}^{N} M_{ij}(t, \Delta t) S_j, \qquad (16)$$

where the elements in the matrix $\mathbf{M}$ represent mass mixing rates. This equation is similar to the transilient turbulence parameterization [Eq. (15)]. However, only a few pathways that represent the dominant mixing scales in the convective boundary layer are considered, resulting in a very sparse transilient matrix (see Fig. 1b) that can be numerically solved much faster than the TTP. Specifically, upward transport originates in the bottommost layer and goes to all layers above in the convective boundary layer. Downward transport goes from each layer to the next lower layer. This simulates rapid upward transport from the surface layer by buoyant plumes and more gradual compensatory subsidence. The calculation of the matrix elements is based on the conservation of sensible heat flux in the vertical direction. If Mu and Md represent upward mixing and downward mixing rates, respectively, then (16) can be rewritten as

$$\frac{\partial S_i}{\partial t} = \text{Mu} S_1 - \text{Md}_1 S_i + \text{Md}_{i+1} S_{i+1} \left(\frac{\Delta \sigma_{i+1}}{\Delta \sigma_i} \right), \quad (17)$$

where $\Delta \sigma$ is the relative mass in or thickness of cell i in a numerical model. The upward and downward mixing rates are estimated using the sensible heat flux. See Pleim and Chang (1992) for details and performance tests of the ACM.

f. Coupling of the surface-layer and the mixed-layer schemes

Coupling between the surface and mixed layers is different with each of the schemes. With the K-theory-

based scheme, turbulent sensible heat flux, friction velocity, and virtual potential temperature of the surface layer are used to calculate the Monin–Obukhov length from which the stability parameter is calculated. Depth of the boundary layer and this stability parameter are used to estimate the eddy diffusivity values in the ABL. With the turbulent kinetic energy scheme, the convective velocity W_*, the friction velocity u_*, and the stability parameter are used to estimate the turbulent kinetic energy and its dissipation rate in the surface layer to provide boundary conditions. In the transilient turbulence parameterization, estimated turbulent fluxes in the surface layer are used to destabilize respective dynamic and thermodynamic parameters, which in turn are used in estimating the nonlocal TKE. In the asymmetric convective model, turbulent sensible heat flux and virtual potential temperature of the lowest two layers are used to estimate the mixing rates. Upward and downward mixing rates are used to perform the vertical mixing in the ABL.

3. Data and numerical simulations

The four boundary layer schemes discussed above are tested for their abilities to simulate the structures of the ABL over a densely vegetated region and a sparsely vegetated (arid) region. Numerical simulations are performed for 12 h for all cases to simulate ABL processes. For the densely vegetated region, observational data from the First ISLSCP (International Satellite Land Surface Climatology Project) Field Experiment (FIFE) are used to perform numerical simulations. The FIFE site is located near Manhattan, Kansas, covering a 15 km × 15 km area where tall grass prairie was the predominant vegetation. Measurements during two of the five intensive field campaigns (IFCs) from the FIFE data (Sellers et al. 1992) are selected to provide initial conditions and for comparison with the model simulations. The starting times of the simulations for these two cases are 1200 UTC 11 July 1987 (0700 LT) and 1200 UTC 6 June 1987. During the IFCs, special efforts were made to measure various meteorological, hydrological, and biological parameters. During these two particular days, which Sellers et al. (1992) list as "golden days," almost clear sky and weak advection conditions were noted. For the sparsely vegetated region, observational data from day 33 (16 August 1967) of the Wangara boundary layer experiment are used to perform simulations. Initial conditions are obtained at 2300 UTC 16 August 1967 (0900 LT).

For the FIFE simulations, single-site radiosonde profiles are used (Pleim and Xiu 1995) in estimating the geostrophic winds. For the Wangara simulations, temporally evolving geostrophic winds are derived for every 3 h from the closely spaced measurements (Mellor and Yamada 1974). The values used for various surface parameters are shown in Table 1. These values are used

TABLE 1. Surface parameter values used in all numerical simulations.

Parameter	FIFE—IFC2	FIFE—IFC1	Wangara
$R_{s\,min}$ (s m^{-1})	60.0	60.0	80.0
LAI	2.80	1.90	0.1
Veg	0.99	0.99	0.05
Texture	Silty clay loam	Silty clay loam	Sand
W_{g1} (m^3 m^{-3})	0.270	0.230	0.155
W_{g2} (m^3 m^{-3})	0.255	0.250	0.155
Z_0 (m)	0.065	0.045	0.0024
T_{g1} (K)	296.0	289.15	279.0
T_{g2} (K)	297.0	293.35	273.0

$R_{s\,min}$: minimum stomatal resistance; LAI: leaf area index; Veg: vegetation cover; W_{g1}: layer 1 volumetric soil moisture; W_{g2}: layer 2 volumetric soil moisture; Z_0: surface roughness length; T_{g1}: layer 1 soil temperature; T_{g2}: layer 2 soil temperature.

for all simulations and are the same as those used by Pleim and Xiu (1995).

4. Results and discussion

The first subsection presents simulation results from the two FIFE cases (for a densely vegetated region), and the second subsection gives results from the Wangara simulations (for a sparsely vegetated region).

a. Simulation of the boundary layer over the FIFE region

1) THE 11 JULY 1987 CASE STUDY

During this day, the second IFC of the FIFE, clear sky conditions were observed until afternoon. Cloud-camera observations indicated overcast sky conditions after 1500 LT. Because the current version of our model does not consider processes related to cloud formation and its effects on atmospheric radiation and surface processes, model predictions after 1500 LT may not be comparable to observations. The temporal variations in the net radiation reaching the ground estimated by the model and from the observations are shown in Fig. 2a. Model estimation of the net radiation is very close to the observations up to 1530 LT; after that, the model estimates deviated because the model does not consider dynamic and thermodynamic processes related to cloud formation. Since the treatment of surface layer processes is the same in all four of the mixed-layer schemes, almost the same net radiation is estimated in all cases (differences among the results are about ±5 W m^{-2}).

Turbulent latent heat fluxes in the model are estimated using the prognostic equations for soil moisture and parameterization of vegetative transpiration (Noilhan and Planton 1989; Jacquemin and Noilhan 1990; Pleim and Xiu 1995). Figure 2b compares these predictions with surface turbulent latent heat fluxes measured using the eddy correlation method. The predicted latent heat fluxes from the four ABL schemes differ from each other by about 0–30 W m^{-2}, even though surface pro-
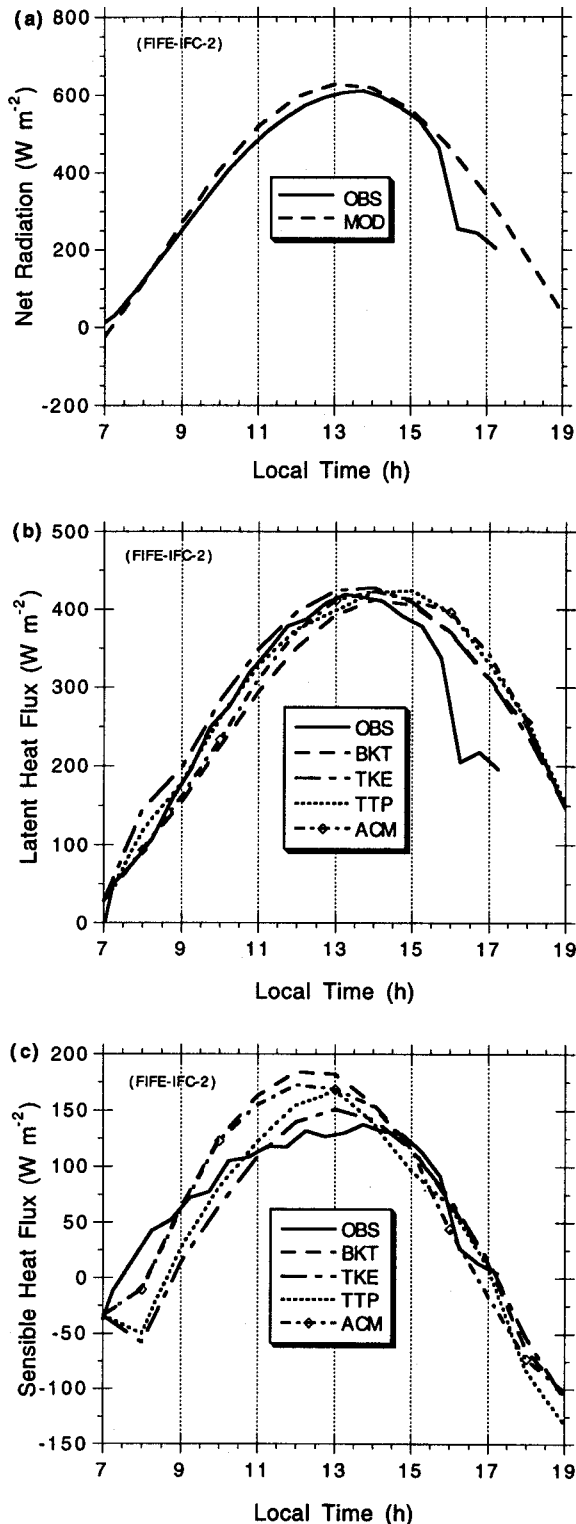
FIG. 2. (a) Temporal variation in the observed and predicted net radiation reaching the ground for the 11 July 1987 FIFE case study. (b) Temporal variation in the observed and predicted turbulent latent heat fluxes for the 11 July 1987 FIFE case study. (c) Temporal variation in the observed and predicted turbulent sensible heat fluxes for the 11 July 1987 FIFE case study.

cesses are represented by a single set of formulations. These differences arise from the different representations of turbulent mixing processes in the four ABL schemes. In other words, turbulent mixing processes can affect surface fluxes by changing gradients across the surface atmosphere interface. Measured latent heat fluxes show a maximum of about 415 W m^{-2} occurring around 1300 LT. Until 1400 LT, TTP-predicted latent heat fluxes are the closest to the observations. However, the differences between the schemes are well within the uncertainty of the measurements. After 1400 LT, predicted values from each of the mixed-layer schemes deviate greatly from the measurements due to cloud effects.

Figure 2c shows the temporal variation in the measured and predicted sensible heat fluxes from the four schemes. Until 1400 LT, predicted sensible heat fluxes from all of the schemes differ from measurements. Sensible heat fluxes are lowest with the TKE scheme and highest with the BKT scheme, with a maximum difference of about 50 W m^{-2}. This is the reverse of the trend in predicted latent heat fluxes (Fig. 2b), where the TKE scheme is highest and the BKT scheme is lowest.

In air quality modeling, accurate specification of near-surface air temperature is crucial. This is because biogenic emission rates, which can influence the formation of ozone in the lower troposphere, are strongly dependent on air temperature. Thus, differences in the predicted air temperatures can result in different estimates of biogenic emission rates. We found that the predicted ground temperature (T_{g1}) is highest with the TTP and lowest with the ACM, with a maximum difference of about 1.5 K. A consistent difference of about 1–2 K between measurements and predictions occurs because the measurement locations of the fluxes and soundings are different from the locations where ground temperatures are measured. Predicted air temperatures in layer 1 ($\sim$11 m AGL) with the TKE scheme and the TTP are closer to each other and to observations. Similarly, predicted air temperatures with the BKT scheme and the ACM are very similar to each other and are about 2–3 K lower than those in the observations.

Figure 3a shows the vertical variation in "observed" virtual potential temperature Θ_v estimated from the observed temperature and water vapor mixing ratio for different observational periods. The presence of the superadiabatic lapse rate, a typical feature during the daytime near the surface, is evident starting from 0900 LT. The stronger vertical gradient (inversion) present at higher altitudes indicates the approximate altitude of the top of the mixed layer in each Θ_v profile. The Θ_v profiles from 1400 LT contain the influence of dynamic and thermodynamic processes related to the reported cloud activity. In the Θ_v profile at 1900 LT, it appears that the top of the mixed layer is pushed to an altitude (1900–2000 m) relatively higher than those in the other profiles. However, this feature cannot be simulated with the current model version.
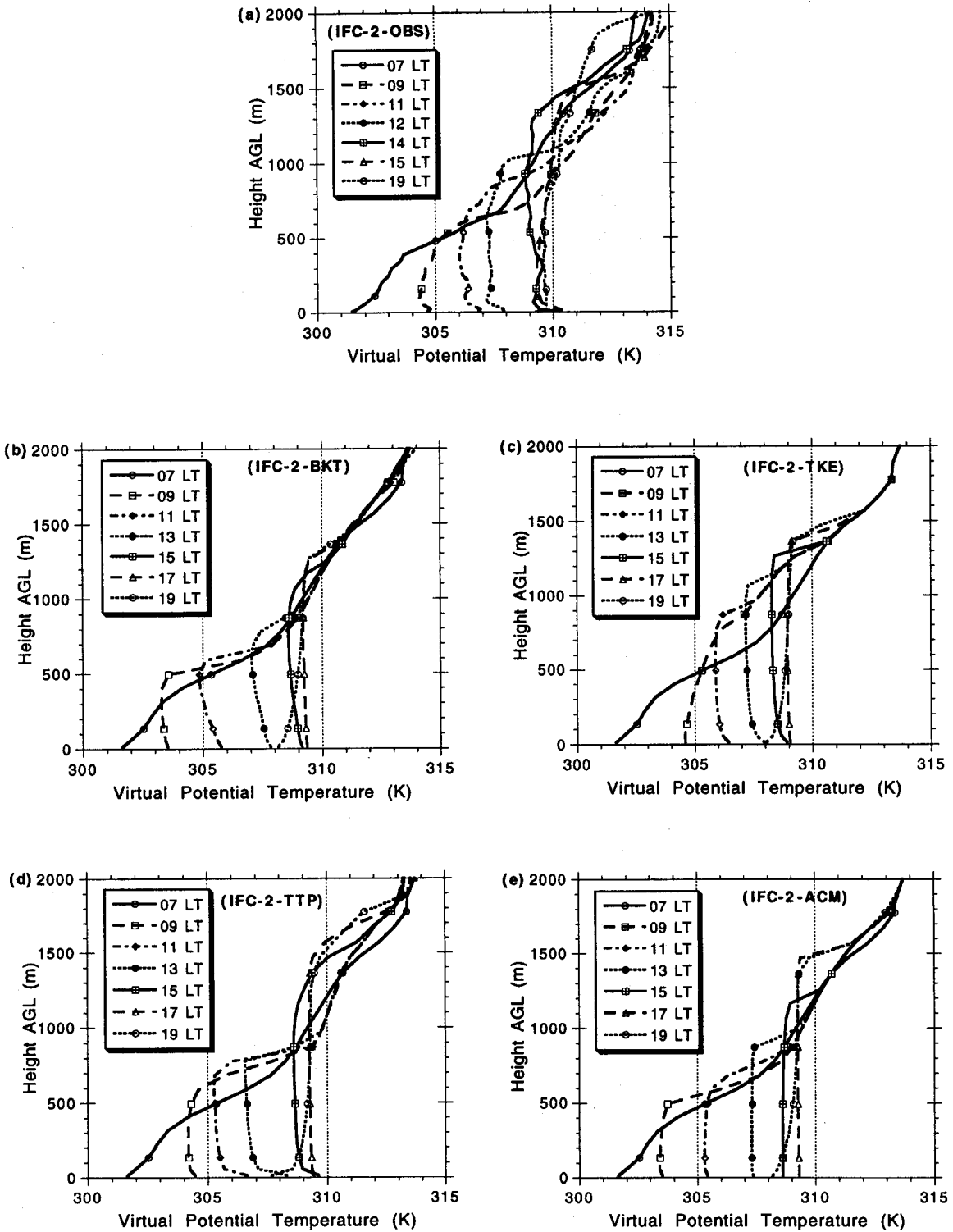
FIG. 3. (a) Vertical variation in the "observed" virtual potential temperature for different observational periods for the 11 July 1987 FIFE case study. (b)–(e) Vertical variation in predicted virtual potential temperature for the 11 July 1987 FIFE case study.

Predicted Θ_v profiles from the four ABL schemes are shown for every 2 h from 0700 LT to 1900 LT in Figs. 3b–e. The vertical profiles at 0700 LT represent initial conditions in all four cases. In the BKT simulation (Fig. 3b), starting from 0900 LT the inversion is located at a lower altitude than in the observations (Fig. 3a). Also, all Θ_v profiles except at 1700 LT in the BKT show the presence of vertical gradients (weak unstable lapse rates) within the ABL, and the BKT scheme does not simulate well the superadiabatic lapse rates near the surface. However, the mean Θ_v of the predicted mixed layer (309.25 K) at 1700 LT is very close to the observed value at 1800 LT (309.5 K). Though observations indicated cloud formation after 1500 LT, predicted Θ_v profiles after 1500 LT are close to the observations. This may be due to the absence of warm- or cold-air advection to the observational site.

In the TKE simulations (Fig. 3c), gradual growth of the mixed layer can be seen from the Θ_v profiles starting from 0900 LT, similar to that in the observations. Unstable lapse rates near the surface indicate the presence of the surface layer. However, these unstable lapse rates are not as strong as in the observations. The vertically uniform predicted Θ_v above the surface layer indicates the presence of a well-mixed layer as found in the observations. The predicted mean Θ_v of the mixed layer at 1700 LT is about 0.5 K lower than the observed value. In the TTP simulations (Fig. 3d), the Θ_v predicted profiles up to 1300 LT show that the altitude of the inversion is still confined to about 800 m, similar to that in the BKT simulations. However, significant growth in the depth of the well-mixed layer is found after 1300 LT. The unstable lapse rates predicted in the surface layer are stronger than in the observations. The mean Θ_v of the mixed layer at 1700 LT is the same as in the observations. The Θ_v profiles in the ACM predictions (Fig. 3e) indicate relatively better growth of the mixed layer as compared to the BKT and TTP simulations. However, unstable lapse rates in the surface layer are very weak compared to observations. The mean Θ_v of the mixed layer at 1700 LT is similar to that in the observations at 1800 LT, with a well-mixed layer present throughout the simulation.

Prediction of stronger unstable lapse rates in the TTP may be due to underestimation of the magnitudes of mixing coefficients in the surface layer. It was also found that the negative sensible heat fluxes (due to entrainment processes) near the altitude of top of the ABL are smaller in the TTP than that in the TKE, particularly until 1300 LT. Hence, erosion of inversion near the altitude of top of ABL is weaker in the TTP as compared to that in the TKE. Thus, in the TTP simulations, neglecting vertical transport of turbulence, underestimating mixing coefficients in the surface layer, and simulating weak entrainment near the altitudes of top of the evolving ABL may have contributed to the slower growth of the ABL until 1300 LT. In a modeling study, Ayotte et al. (1996) compared the normalized turbulent fluxes obtained from

a large eddy simulation model with those obtained from some local- and nonlocal-closure schemes used in general circulation models. In one of the several case studies, they also found that all of the ABL schemes (including the TTP) used in their one-dimensional model could not reproduce the entrainment fluxes as compared to those in the LES. Thus, differences in the predicted Θ_v among the simulations can be attributed in part to the differences in the entrainment fluxes.

In the BKT and ACM simulations, the altitude of the top of the mixed layer must be diagnosed from wind and temperature profiles. We use the bulk Richardson number criterion, similar to that used by Pleim and Xiu (1995) and suggested by Holtslag et al. (1990), in determining the depth of the ABL. On the other hand, specification of the depth of vertical mixing is not required in the TKE and TTP simulations. This is because in the absence of clear air turbulence, the turbulent kinetic energy becomes negligibly small ($\sim 1.0 \times 10^{-20}$ m^2 s^{-2}) in the TKE simulations near the top of the mixed layer. Similarly, in the TTP simulations off-diagonal elements in the transilient matrix become zero at altitudes near and above the top of the mixed layer. In the BKT simulations, the Θ_v profiles in the ABL indicate that the vertical mixing is underestimated in the mixed layer and overestimated in the surface layer. This is a typical characteristic of local-closure schemes in which vertical transport is proportional to vertical local gradients. Therefore, to achieve a well-mixed profile, vertical eddy diffusivity must go toward infinity. Further, the calculated altitude of the top of the mixed layer seems to be underestimated. In the ACM simulations, turbulent mixing rates in the ABL are determined by the magnitude of the sensible heat flux at the prespecified top of the surface layer and the potential temperature difference between layers 1 and 2 using an empirical formula. Therefore, the magnitude of the superadiabatic surface layer is dependent on the thickness of the lowest model layer. The main advantage of the ACM over the BKT in convective conditions is that the nonlocal mixing results in very uniform mixed layers without resorting to extraordinarily large eddy diffusivities or very short time steps in a numerical simulation.

Vertical profiles of observed horizontal winds (not shown) indicate the presence of a nocturnal jet in the stable boundary layer at 0700 LT. Thus, shear production of turbulence is probably an important factor in the growth of the ABL during the morning hours by causing mixing through the capping inversion. This process is accounted for in the TKE and the TTP simulations. While the mixing rates of the ACM and the BKT do not directly respond to vertical wind shear, the specification of the ABL top depends on the local wind shear across the interface of the inversion. Therefore, as these schemes are integrated in time, vertical wind shear at the top of the ABL increases the modeled depth of the ABL, thus including part of the capping inversion in a more rapidly mixing ABL. In this way the inversion is

eroded over time allowing ABL growth. Clearly, as shown in Figs. 3 and 4, the morning ABL growth is slower for the BKT than the ACM because the local mixing in the stable entrainment zone is much less than the nonlocal convective mixing in the ACM.

In the absence of cloud formation and advection processes, the vertical distribution of trace gas species in the lower troposphere is largely controlled by ABL processes. The water vapor mixing ratio can be considered as a surrogate for the trace gas species (nonreactive) (just as latent heat fluxes at the surface can be viewed as a surrogate for surface emission fluxes). Thus, the temporal behavior and vertical distribution of the water vapor mixing ratio q_v can provide some insight on the probable behavior of a surface-emitted nonreactive trace gas species. Vertical profiles of observed q_v at different hours are shown in Fig. 4a. Except at 1400 and 1800 LT, q_v profiles indicate a uniform distribution within the mixed layer. Larger gradients can be seen in the surface layer. These gradients in the surface layer may be due to errors in the measurements in the surface layer (0–100 m) and/or to the presence of large latent heat fluxes ($\sim$450 W m^{-2}) as seen in Fig. 2b. The mean q_v inside the ABL changes from hour to hour, both increasing and decreasing, in ways that cannot be explained by vertical mixing and surface fluxes alone. Therefore, one-dimensional models cannot possibly replicate all of these observed features.

Vertical variation in q_v at different hours of simulation with the four schemes are shown in Figs. 4b–e. In the BKT simulations (Fig. 4b), vertical gradients of q_v are present in the ABL during the entire period of simulation as a result of weaker vertical mixing. For example, the q_v profile at 1500 LT varies from 16.5 g kg^{-1} at the surface to 11 g kg^{-1} at 1200-m altitude while the observations (Fig. 4a) indicate a uniform value of 16 g kg^{-1} in the mixed layer (up to 1400-m altitude). Further, due to the availability of large latent heat fluxes and BKT's slower growth of the mixed layer as compared to the observations, the mean q_v of the mixed layer increases for the period 0700–1200 LT. Turbulence in the free atmosphere is parameterized using Eq. (13) in the BKT and ACM simulations. Variations in the BKT-predicted q_v above the ABL (1500 m) are due to the free atmospheric turbulence and somewhat resemble those in the observations. In the TKE simulations (Fig. 4c), vertical variation in q_v indicates almost uniform profiles within the ABL except at 0900 LT. Rapid growth of the mixed layer (shown later in Fig. 5) at 0900 LT in the TKE simulations causes overprediction of q_v between the 700- and 1200-m altitudes. In the surface layer (0–100 m), the TKE simulations also show the presence of vertical gradients in q_v. However, these are weaker than in the observations. Above the ABL (1500 m), the TKE scheme did not simulate free atmospheric turbulence, resulting in no changes in q_v during the entire simulation period.

Vertical variation in q_v in the TTP simulations (Fig.

4d) indicates slower development of the ABL until 1300 LT. After 1300 LT, predicted q_v profiles also indicate a sudden growth of the ABL, which results in a decrease of the mean q_v in the ABL as compared to that at 1300 LT. In the surface layer, strong vertical gradients in q_v are predicted by the TTP and are very similar to the observations. Temporal variations in q_v in the free atmosphere (altitudes above the ABL) are also present in the TTP simulations. Vertical variation in q_v in the ACM simulations (Fig. 4e) indicates somewhat mixed results compared with the other simulations. Mean values of q_v in the ABL during the entire period of simulation (except at 1900 LT) are very similar in the ACM.

Observed eastward and northward wind velocity profiles (not shown) indicate the presence of remnants of a nocturnal jet in the lower altitudes in the initial conditions (0700 LT). Presence of vertical wind shear in the ABL (an indication of weaker vertical mixing) and slower growth of the mixed layer are found in the BKT simulations. The TKE simulations (not shown) indicate that the altitude of the maximum wind in the ABL ($\sim$1000 m) is higher than in the BKT simulations. In the TTP simulations (not shown), vertical wind shear associated with the nocturnal jet is largely reduced by 0900 LT, similar to the TKE simulations. In the ACM simulations, the wind profiles are somewhat similar to those in the BKT simulations. In general, the effects of differing growths of the mixed layer in each of the simulations are evident in the predicted u and v wind profiles.

The depth of the ABL is a key input in air quality simulation models. Errors in its specification can significantly affect the predicted concentration fields. In the TKE scheme and the TTP the top of the ABL is diagnosed from a TKE criterion, while in the BKT scheme and ACM top of the ABL is specified from the temperature and wind profiles using the bulk Richardson number as described above. Therefore, accurate specification of the ABL height is crucial to these schemes since it determines the vertical extent of the convective mixing. Figure 5 shows the temporal evolution of the depth of the boundary layer. The bulk Richardson number criterion (Holtslag et al. 1990) is used to estimate the depth of the ABL in the BKT and ACM simulations. Since measured depths of the mixed layer are not available, the above methodology is also used to estimate the actual depth of the ABL (referred to as "OBS" in Fig. 5) using the observed winds and temperature profiles. Except for 1100 LT and 1300 LT, the TTP shows higher ABL depths than the other schemes do. In general, all schemes except the TTP predict lower values for ABL depth than the "observed" values. The maximum difference among the schemes for the predicted ABL depths is about 600 m, which translates to about 33% of the maximum predicted depth. Thus, variations in the predicted/estimated depths of the ABL may influence air quality simulation results.
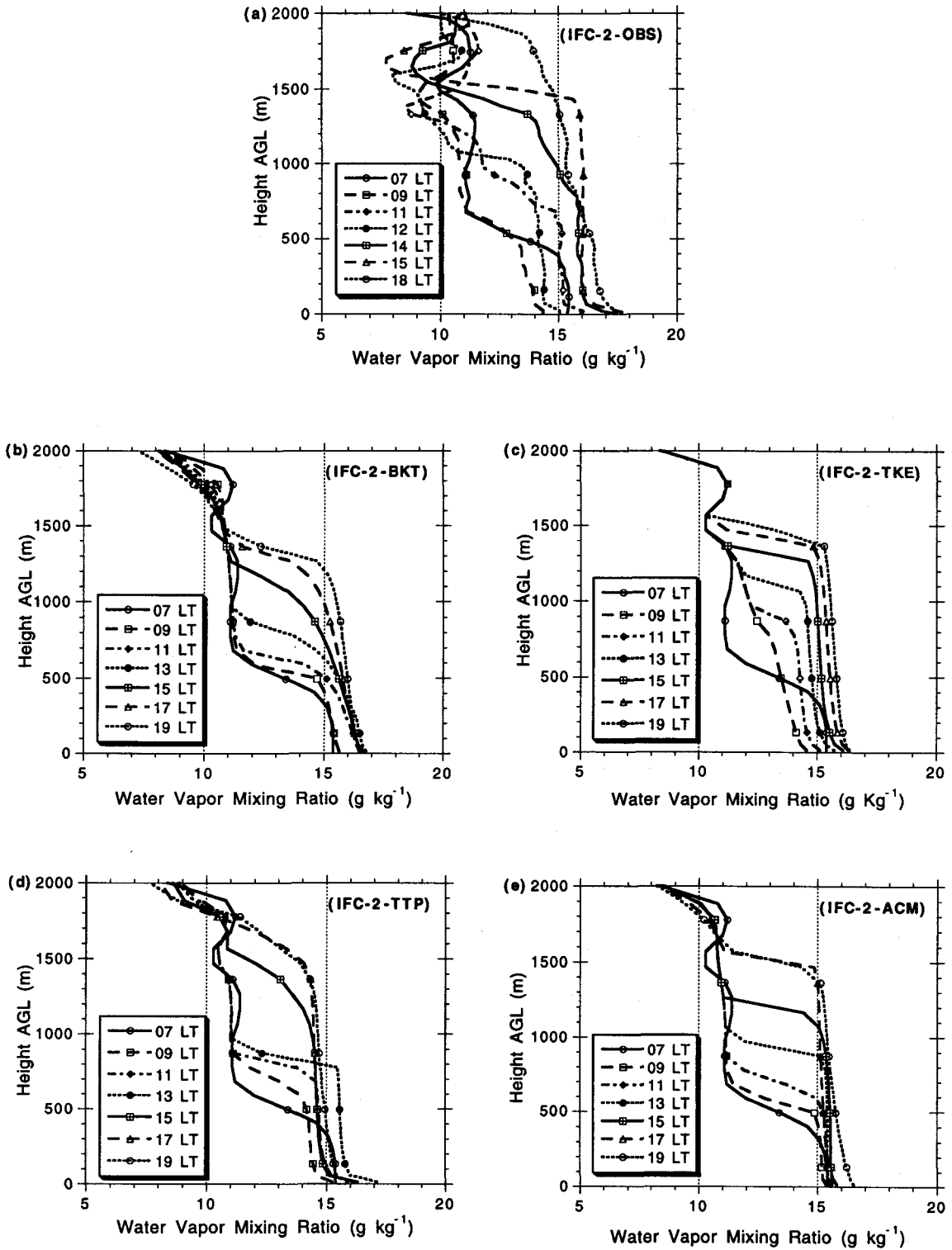
FIG. 4. (a) Vertical variation in observed water vapor mixing ratio for different observational periods for the 11 July 1987 FIFE case study. (b)–(e) Vertical variation in predicted water vapor mixing ratio for the 11 July 1987 FIFE case study.
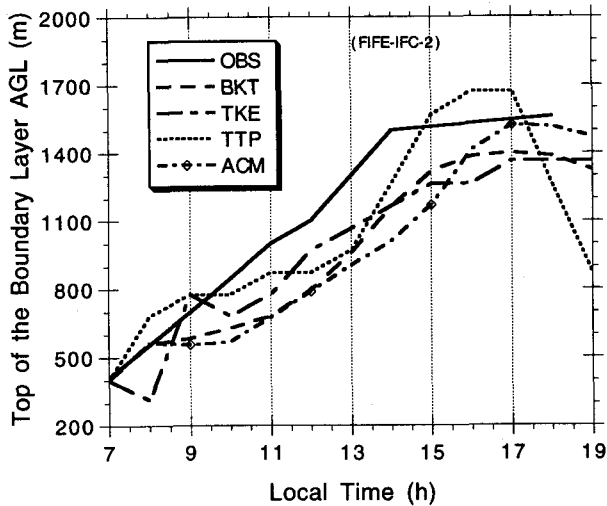
FIG. 5. Temporal evolution of the estimated and predicted depth of the mixed layer for the 11 July 1987 FIFE case study.

2) THE 6 JUNE 1987 CASE STUDY

During our second case study, the first IFC of the FIFE, clear sky conditions were observed during the entire period of simulation. Thus, comparing the measured net radiation with the model estimates will reveal errors in the radiation formulations, initial specification of surface, and atmospheric characteristics (e.g., albedo, emissivity). We found that the model estimates are very close to the observations. This indicates the accuracy of surface input data and the model formulation of radiative processes for clear sky conditions. Next we consider model prediction of turbulent sensible and latent heat fluxes. Figure 6a shows measured and predicted sensible heat fluxes. In general, peak values of predicted sensible heat fluxes in all simulations are higher than

the measurements by about 15–40 W m^{-2}. Though the initial conditions and the formulation used to represent surface layer processes are the same in all of the simulations, the slight differences among the predictions indicate the effects of different representations of turbulent mixing processes. Analogous differences in the predicted latent heat fluxes (Fig. 6b) are smaller.

Of interest to meteorological and air quality simulation modelers is better prediction of near-surface winds, because these can affect the estimation of surface turbulent fluxes of thermodynamic parameters and chemical species. We compare surface observations of u and v winds with the model-predicted winds in the lowest layer (Figs. 7a and 7b). Since the lowest level in the model is located at about 10.9 m AGL, predicted winds can be directly compared to the measurements made at 10 m AGL. Except for the first 2 h of simulation, the trends in the predicted winds in all simulations follow the observations closely. On average, the TTP-predicted winds are closest to the observations, and the ACM predictions are the farthest from observations (overprediction).

We also compared predicted vertical variation in Θ_v with the observations at different hours (not shown). Compared with observations, superadiabatic lapse rates in the surface layer are lower in the BKT and ACM simulations, higher in the TTP simulations, and comparable in the TKE simulations. A feature associated only with the TKE simulations was the prediction of mixing in the residual boundary layer between 0700 and 0900 LT as observed. We also found that warming of the ABL (as indicated by the Θ_v profiles) is different in each of the simulations until 1300 LT, indicating the effects of different mixing schemes on the predicted ABL.

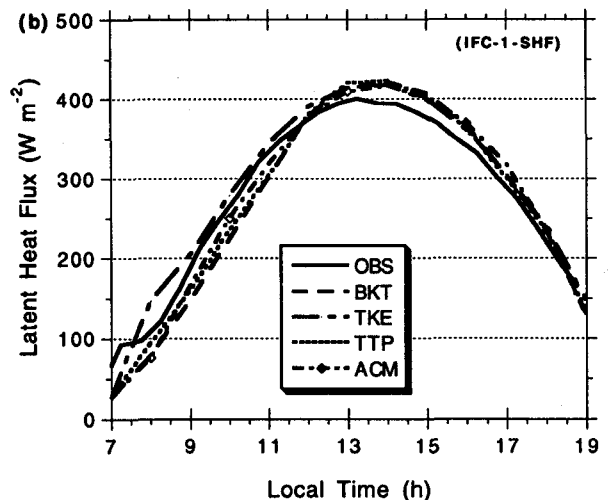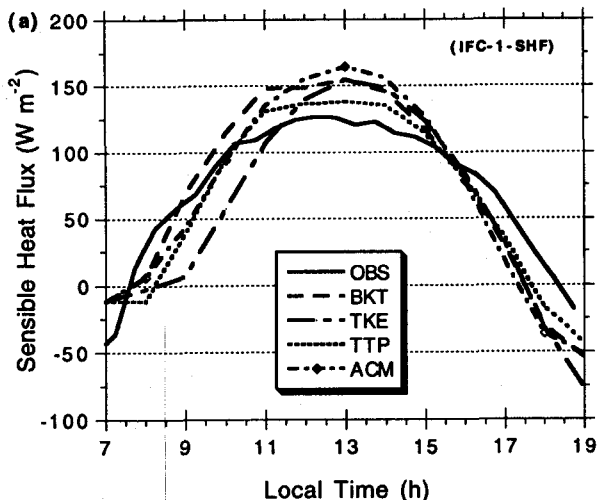Predictions of the horizontal winds in a one-dimen-

FIG. 6. (a) Temporal variation in the observed and predicted turbulent sensible heat fluxes for the 6 June 1987 FIFE case study. (b) Temporal variation in the observed and predicted turbulent latent heat fluxes for the 6 June 1987 FIFE case study.
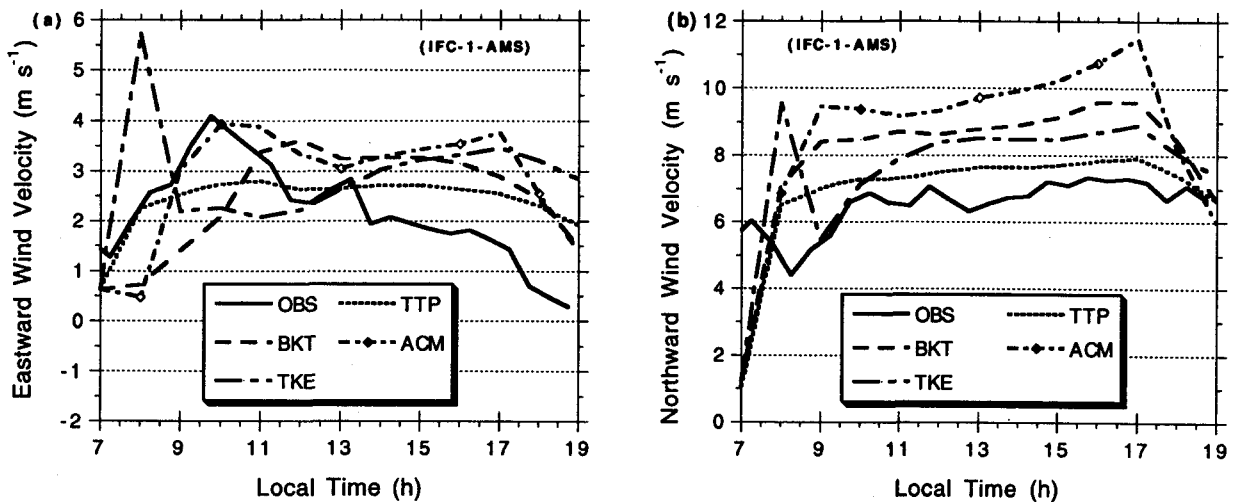
FIG. 7. (a) Temporal variation in the observed and predicted u wind near the surface ($\sim$10 m AGL) for the 6 June 1987 FIFE case study. (b) Temporal variation in the observed and predicted v wind near the surface ($\sim$10 m AGL) for the 6 June 1987 FIFE case study.

sional model are very sensitive to the prescribed geostrophic wind profiles. In all of our simulations we prescribe geostrophic wind profiles that were used by Pleim and Xiu (1995). Since horizontal pressure gradients are not readily available, they used a qualitative procedure to estimate temporally evolving geostrophic winds. Vertical variation in the u wind (eastward component) obtained from observations is shown in Fig. 8a. Again, the presence of a nocturnal jet at 0700 LT is evident from the u wind profile between the surface and 1000-m altitude; the core of the jet is located at about 500 m AGL. The u wind profile at 1600 LT shows the presence of a weaker vertical wind shear, indicating the effects of stronger turbulent mixing processes. Figures 8b–e show the predicted u wind profiles from the four ABL schemes. With time, all schemes except the TKE scheme show a gradual decrease in the vertical wind shear in the ABL, similar to the observations. With the TKE scheme, the coefficient of eddy diffusivity for momentum seems to be overestimated; as a result, vigorous vertical mixing leads to well-mixed u wind profiles from 0900 LT on. After 1300 LT, differences among the predicted u winds are about ± 1 m s^{-1} in all simulations.

Vertical variation in the v wind (northward component) is shown in Fig. 9a. The presence of the nocturnal jet is somewhat evident (0700 LT) in the lower altitudes of the atmosphere. Also note that the v winds are uniform with height for all of the observational periods. Predicted v wind profiles for the four schemes are shown in Figs. 9b–e. Again, with the TKE scheme vigorous vertical mixing results in a well-mixed v profile above 200-m altitude by 0900 LT. With the other schemes, the decrease in vertical shear in the v winds is more gradual in time, similar to the observations.

Figure 10 shows the temporal variation in the depth of the ABL. As before, observed winds and temperature data were used to estimate the probable altitude of the

top of the ABL utilizing the diagnostic formulation suggested by Holtslag et al. (1990). During the morning period, all of the ABL schemes underestimate the "observed" ABL depths. Among the predicted depths of the ABL, the BKT depth is the lowest in comparison with the observations and the TTP depth is the highest. The maximum difference among the predicted ABL depths is about 250 m.

b. Simulation of the boundary layer over the Wangara region

Because of the high density of the observational network and the availability of many meteorological parameters, the Wangara data have been used in many model comparison and evaluation studies. These data are perhaps the most widely used observational data for comparison with modeled boundary layer structures. Since the Wangara observational site is located over a sparsely vegetated region (close to a desert), errors arising from the insufficient representation of vegetation–atmosphere interactions should be at a minimum in a numerical simulation of the ABL. This feature facilitates the evaluation of other meteorological fields simulated in a numerical model. Since we have used all available observational data to specify initial values for various surface characteristics and parameters, the same soil-vegetation model that was utilized in the FIFE simulations is used for the Wangara case study.

We found that the predicted net radiation is slightly higher than observed around 1200 LT by about 30 W m^{-2}. Predicted negative values during the nighttime are also close to the observations. We compared temporal variation in the predicted sensible heat fluxes with that derived from observations (Hicks 1981). Between 0900 and 1100 LT, differences between the derived and predicted sensible heat fluxes are found. This kind of dis-
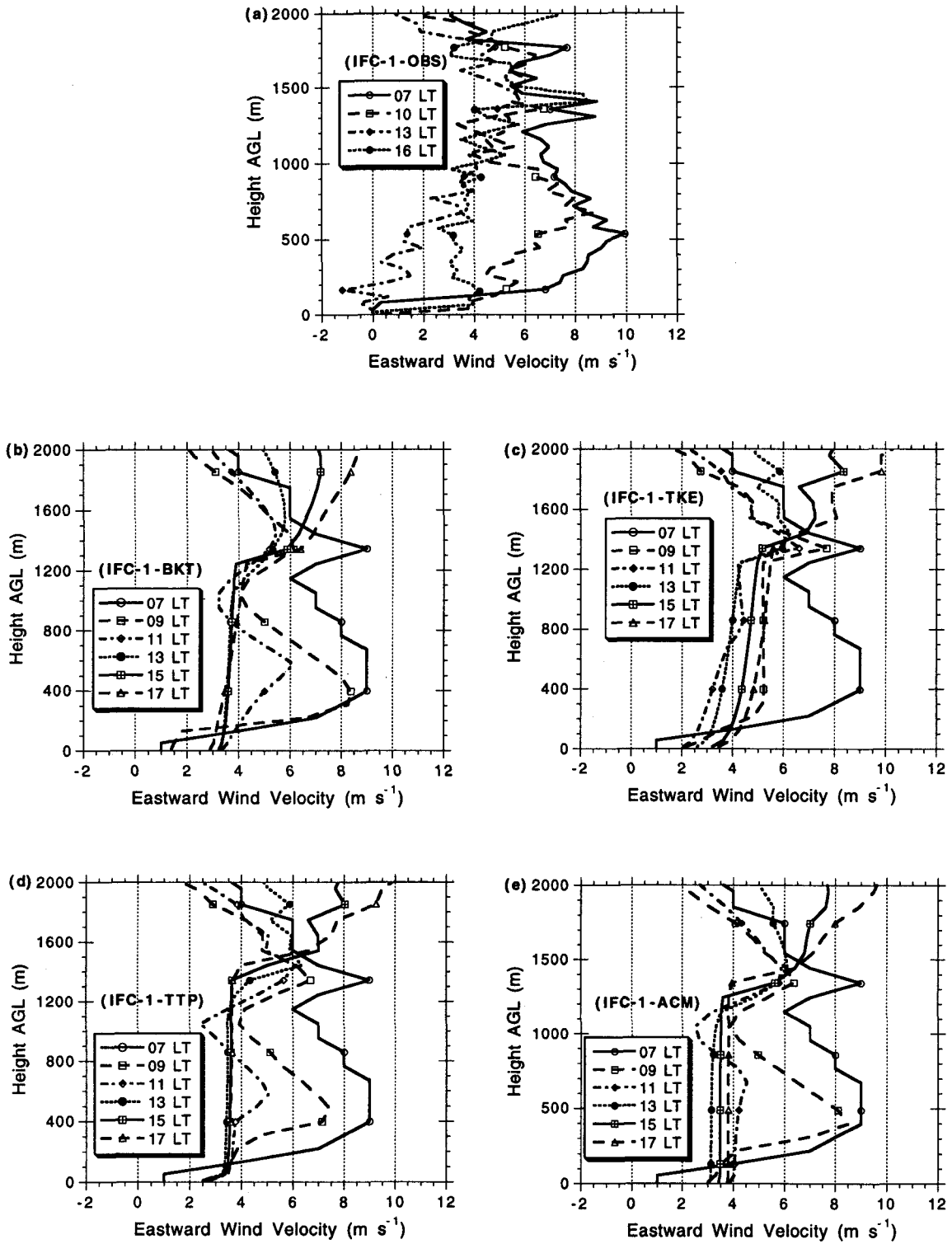
FIG. 8. (a) Vertical variation in observed eastward wind velocity (u wind) for different observational periods for the 6 June 1987 FIFE case study. (b)–(e) Vertical variation in predicted eastward wind velocity (u wind) for the 6 June 1987 FIFE case study.
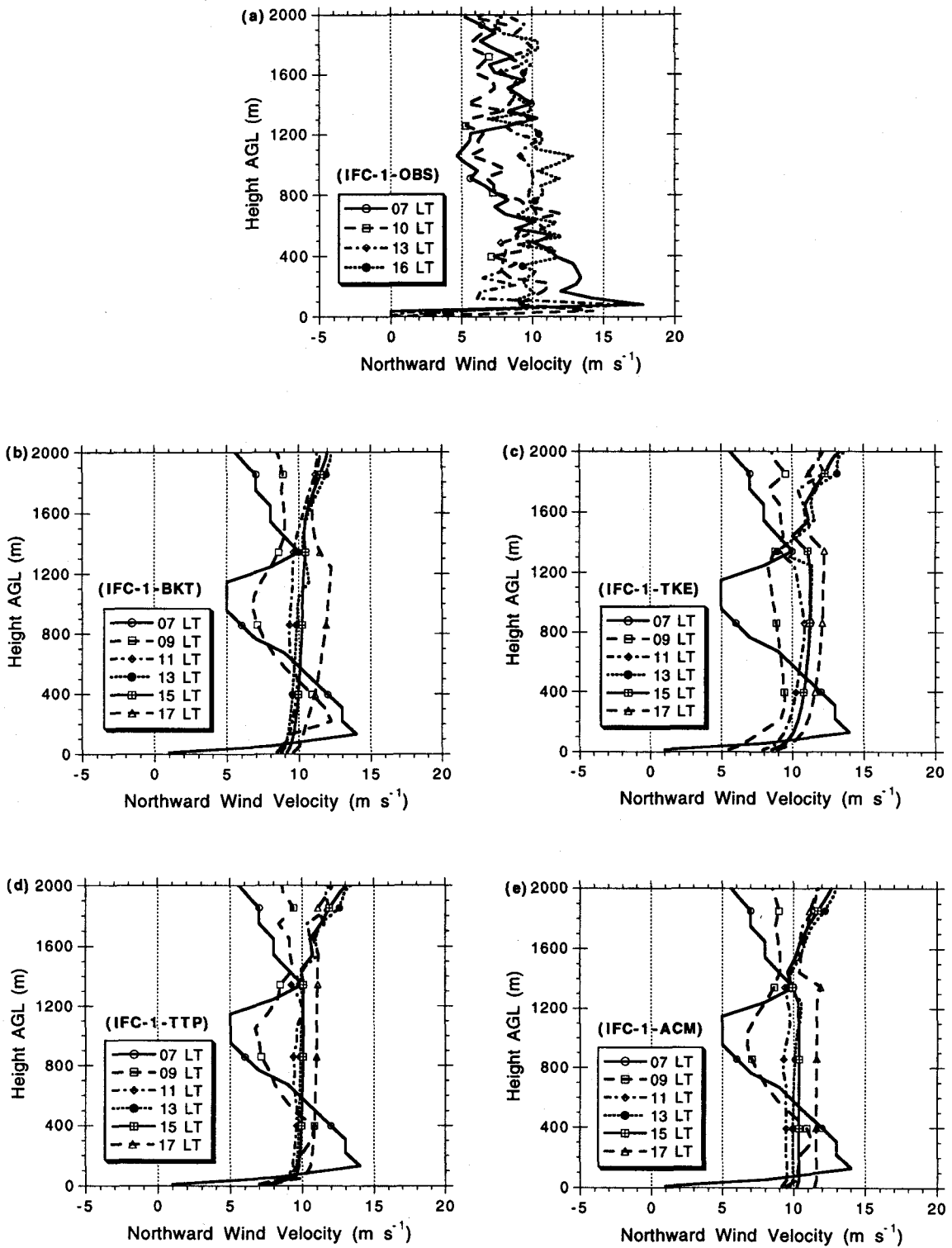
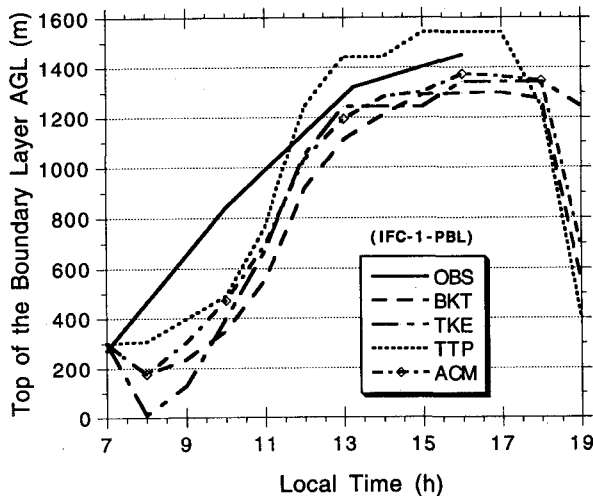FIG. 9. (a) Vertical variation in observed northward wind velocity (*v* wind) for different observational periods for the 6 June 1987 FIFE case study. (b)–(e) Vertical variation in predicted northward wind velocity (*v* wind) for the 6 June 1987 FIFE case study.

FIG. 10. Temporal evolution of the estimated and predicted depth of the mixed layer for the 6 June 1987 FIFE case study.

crepancy was also found between the values reported by Hicks (1981) and modeled by Mellor and Yamada (1974). Except between 1200 and 1400 LT, predicted sensible heat fluxes from the four ABL schemes are very similar to each other.

Figures 11a and 11b show vertical profiles of observed and predicted u and v winds at 1200 LT. Note that the differences among the predicted wind profiles are very small (less than 0.5 m s^{-1}) and predicted winds are close to the observations. The observed and predicted wind profiles at 1800 LT shown in Figs. 11c and 11d have similar features, except the predicted v wind profiles differ from the observed. This kind of difference, which was also noticed in the simulation performed by Mellor and Yamada (1974), may be due to errors in the estimation of geostrophic winds for this hour. Figure 12a shows the vertical profiles of Θ_v obtained from observations for different periods. The Θ_v profile at 0900 LT shows the presence of a stable boundary layer, about 400 m deep. From 1200 to 1500 LT, the mean mixed layer warms up by about 2.5 K. At 2100 LT a stable boundary layer is established as indicated by a strong gradient (8 K) between the surface and 100-m altitude. Corresponding model predictions are shown in Figs. 12b–e. As indicated by the Θ_v profile at 1200 LT between the altitudes 800 m and 1200 m, the TKE scheme predicts an ABL depth at this hour that is lower than in the other schemes and the observations. Again, differences among the predictions from the four ABL schemes show up in the surface layer and at altitudes near the top of the mixed layer. Warming of the ABL from 0900 to 1200 LT by about 2.5 K is well predicted by all of the schemes. Development of a stable boundary layer during the nighttime (2100 LT) is also well predicted by all ABL schemes. Since the ACM cannot be used during stable conditions, K theory is used to simulate the ABL processes. Even though model

simulations with the BKT scheme and the ACM use the same K theory at 2100 LT, the predicted stable boundary layer is quite different between the two schemes. This is due to differences in the predicted vertical mixing processes during daytime conditions between these two schemes.

Observed water vapor mixing ratio profiles for different hours (not shown) indicate that the growth of the ABL during the daytime results in well-mixed q_v profiles except at 2100 LT. Both the Θ_v and the q_v profiles at 2100 LT suggest advection of cold and humid air into the observational site. Since advection is not considered in the numerical simulations, predictions corresponding to this hour differ slightly from the observations. We found that the ACM-predicted profiles are closest to the observations. Again, most of the differences among the predictions occur at altitudes close to the surface and near the top of the mixed layer. Further, the TTP does not predict the changes in q_v at altitudes near the top of the mixed layer that are found in the observations and in the predictions from the other ABL schemes.

Figure 13 shows the temporal variations in the predicted and observed depths of the ABL. The TTP predicts a deeper mixed layer while the TKE scheme shows weaker growth until 1500 LT. The dramatic collapse of the ABL is well predicted with all of the ABL schemes. However, the collapse in the observations occurs between 1600 and 1800 LT while in the predictions it occurs about 1–2 h earlier. Overall, the ACM shows the best agreement with the observations.

5. Conclusions

We have studied the performance of two local-closure and two nonlocal-closure boundary layer schemes in simulating the observed structures of the ABL over densely and sparsely vegetated regions using a one-dimensional soil–vegetation–boundary layer model. The local-closure schemes used in the study are (1) a K-theory-based scheme using boundary layer scaling (BKT) and (2) a scheme based on turbulent kinetic energy and its dissipation rate (TKE). The nonlocal-closure schemes are (1) the transilient turbulence parameterization (TTP) and (2) the asymmetric convective model (ACM). Two of these schemes are based on the TKE equation (TKE and TTP) and apply to the entire vertical column while the other two schemes (BKT and ACM) parameterize mixing within the boundary layer and above differently and therefore depend on the specification of ABL height. Since the TKE scheme contains the most complete physics, including both dynamic and thermodynamic effects, features such as the presence of superadiabatic lapse rates in the surface layer as well as vertical mixing resulting from strong vertical wind shear associated with the dissipating nocturnal jet are well reproduced by the TKE scheme. Thus, TKE-predicted temperature, water vapor mixing ratio, and horizontal wind profiles are generally consistent with ob-
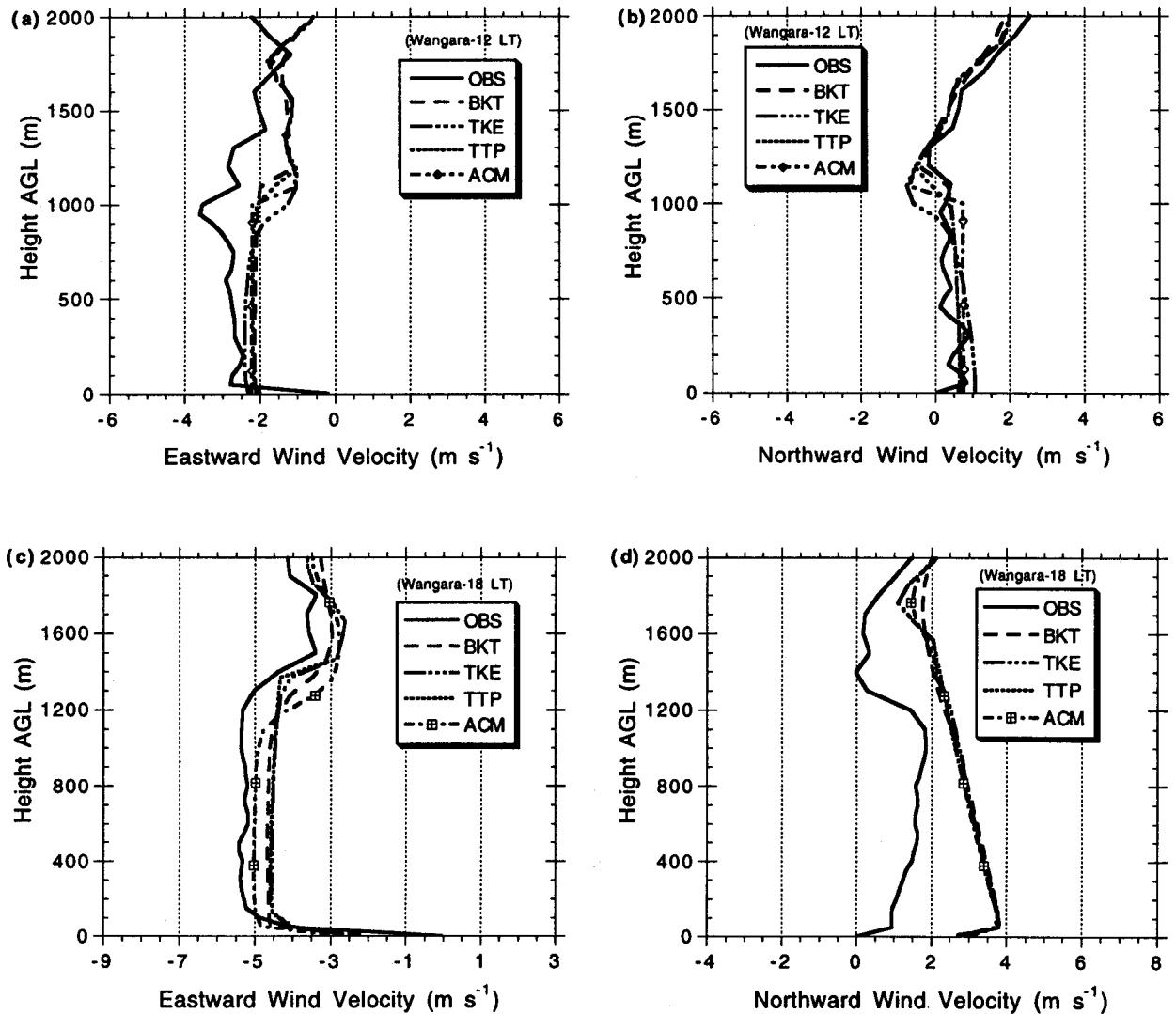
FIG. 11. (a) Vertical profiles of observed u wind at 1200 LT and corresponding predicted profiles for the Wangara simulations. (b) Vertical profiles of observed v wind at 1200 LT and corresponding predicted profiles for the Wangara simulations. (c) Vertical profiles of observed u wind at 1800 LT and corresponding predicted profiles for the Wangara simulations. (d) Vertical profiles of observed v wind at 1800 LT and corresponding predicted profiles for the Wangara simulations.

servations. In general, the TTP-predicted depths of the boundary layer are larger than with the other schemes, and the superadiabatic lapse rates are stronger than in the observations.

In the BKT scheme and the ACM, the depth of the boundary layer has to be diagnosed using empirical formulations. Since the coefficients for vertical eddy diffusivity are strong functions of the depth of the boundary layer in the BKT scheme, errors in the specification of this depth greatly influence BKT-predicted vertical mixing. Thus, errors in the predicted temperature, mixing ratio, and horizontal wind profiles with the BKT scheme can be attributed in part to errors in the estimated ABL depth. In one of the three case studies, the presence of vertical gradients in the predicted profiles

of temperature, mixing ratio, and winds indicates that mixing is weaker in the upper half of the evolving mixed layer. Further, the presence of strong vertical mixing in the lower layers close to the ground results in the prediction of weaker superadiabatic lapse rates in the surface layer with the BKT scheme.

The ACM performs upward mixing throughout the depth of the ABL, while downward mixing is gradual. The effects of this feature are clearly evident in all simulations where the predicted dynamic and thermodynamic profiles indicate a well-mixed boundary layer. However, vertical mixing in the ACM may be overestimated in the lowest layers, leading to weak adiabatic lapse rates in the surface layer. It is interesting to note that estimated depths of mixed layer are not the same
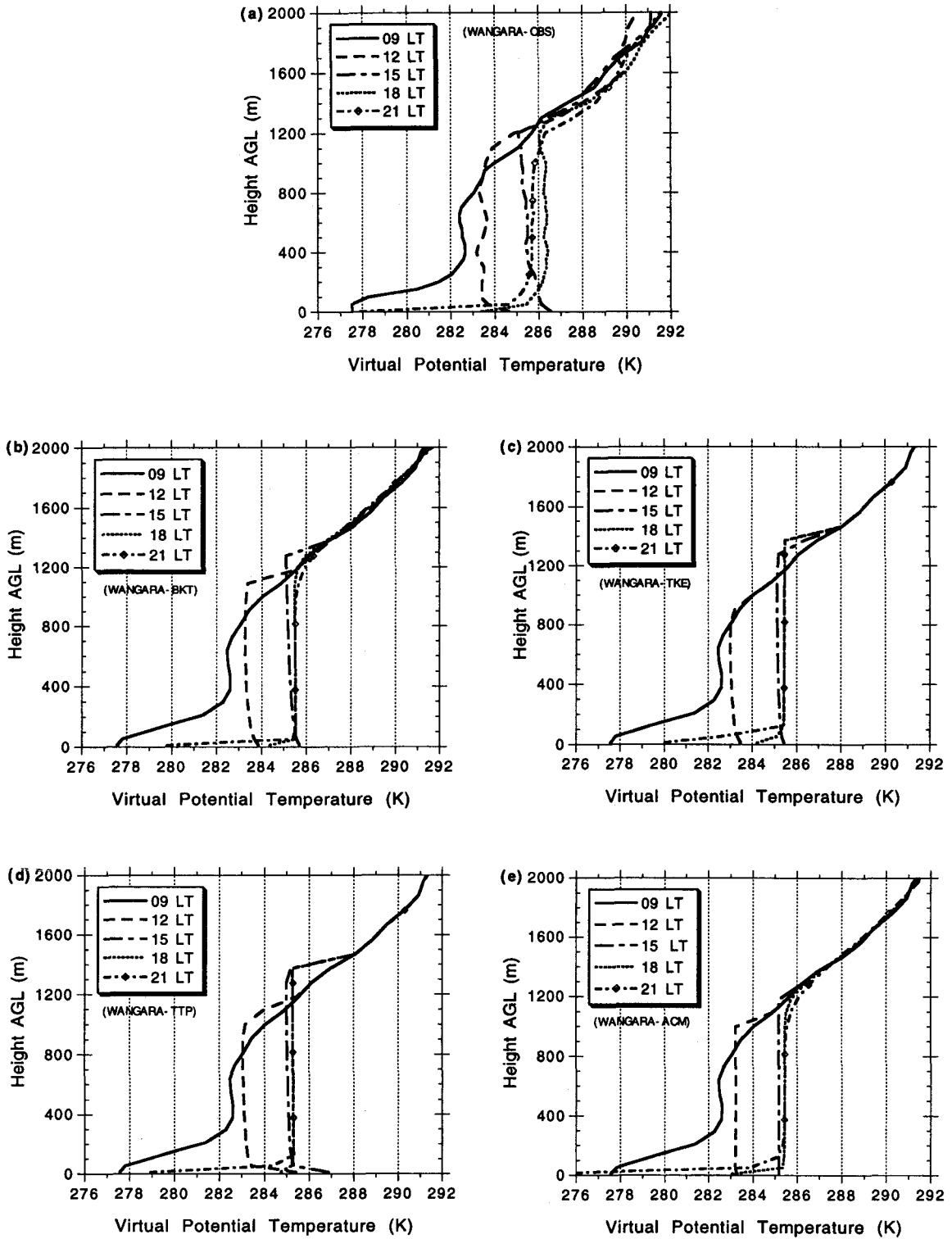
FIG. 12. (a) Vertical variation in "observed" virtual potential temperature for different observational periods for the Wangara simulations. (b)–(e) Vertical variation in predicted virtual potential temperature for the Wangara simulations.
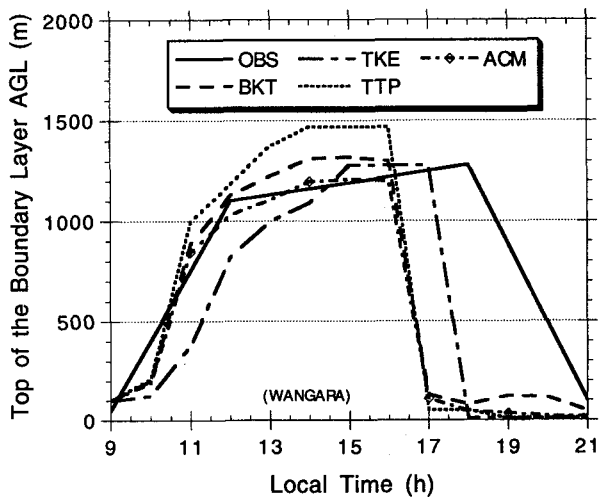
FIG. 13. Temporal evolution of the estimated and predicted depth of the mixed layer for the Wangara simulations.

in the BKT and the ACM even though we used the same formulation (Holtslag et al. 1990) in both of these simulations. This is due to the fact that the virtual potential temperature (Θ_v) difference between the surface layer and the top of the ABL in the BKT and the ACM simulations are not the same due to the differing representations of vertical mixing. This difference in Θ_v directly affects the estimation of the depth of the ABL. Also, simulated depths of the ABL in the ACM are generally closer to the observations than those in the BKT. The largest difference among the predicted depths of the mixed layer was about 33% of the maximum predicted depth.

The TTP computes the mixing fractions, using the model-simulated dynamic and thermodynamic profiles, to reflect the complex interaction among surface heating, buoyant plumes, shear across the boundary layer, and entrainment in the interfacial layer. The ACM also performs mixing from the surface level to all other levels in the boundary layer using empirically estimated mixing rates. However, the design of the mixing in the ACM is entirely different from that in the TTP. In principle, for convective conditions, these schemes should perform the best in simulating the observed structures of the convective boundary layer. However, prediction errors could arise from the uncertainty present in the prescribed constants and/or assumptions related to the simplification of the closure problem. For these reasons in part, mixing of air in the lowest layers is underestimated in the TTP, leading to the prediction of strong superadibatic lapse rates in the surface layer. Similarly, with the ACM, estimation of large mixing rates has caused excessive mixing of air in the surface layer, leading to a prediction where superadiabatic lapse rates are almost absent in the surface layer. Thus, depending upon our ability to estimate key parameters used in a closure

problem, simulation results may or may not be in line with all the observed aspects.

Even though the same surface-layer parameterization scheme is used in all simulations, predicted turbulent fluxes near the surface are marginally different for each of the four schemes. This is caused by the differences in predicted vertical mixing among the schemes, which show that surface turbulent fluxes are influenced by the mixing processes in the boundary layer. Most of the differences in the predicted profiles from each of these schemes are evident during the growing stage of the boundary layer. However, prediction errors are at a minimum when the depth of the boundary layer has attained its maximum growth. We also found that for each of the four schemes, the differences between predictions and observations, which are most evident in the surface layer and near the top of the mixed layer, were consistent across the three studies throughout the simulation periods.

A comprehensive evaluation of the performance of these four mixed-layer schemes requires simulation of boundary processes and associated mesoscale circulations in a three-dimensional model. This is because boundary layer processes can affect shallow and deep cloud formation. In turn, each of these can result in feedback effects, through variations in the solar radiation and in the soil moisture, modulating the simulated mesoscale circulations. Therefore, our next step is to evaluate these schemes using the MM5 (Grell et al. 1994) modeling system.

REFERENCES

Alapaty, K., S. Raman, and R. V. Madala, 1994: Investigation of the role of the boundary layer processes in an active monsoon using a mesoscale model. *Bound.-Layer Meteor.,* **67,** 407–426.

Anthes, R. A., E.-Y. Hsie, and Y.-H. Kuo, 1987: Description of the Penn State/NCAR Mesoscale Model Version 4 (MM4). NCAR Tech. Note NCAR/TN-282+STR, 66 pp. [Available from NCAR, MMM Division, P.O. Box 3000, Boulder, CO 80307.]

Ayotte, K. W., and Coauthors, 1996: An evaluation of neutral and

convective planetary boundary-layer parameterizations relative to large eddy simulations. *Bound.-Layer Meteor*, **79**,131–175.

Blackadar, A. K., 1976: Modeling the nocturnal boundary layer. Preprints, *Third Symp. on Atmospheric Turbulence, Diffusion, and Air Quality*, Raleigh, NC, Amer. Meteor. Soc., 46–49.

——, 1979: Modeling pollutant transfer during daytime convection. Preprints, *Fourth Symp. on Turbulence, Diffusion, and Air Pollution*, Reno, NV, Amer. Meteor. Soc., 443–447.

Businger, J. A., J. C. Wyngaard, Y. Izumi, and E. F. Bradley, 1971: Flux–profile relationship in the atmospheric surface layer. *J. Atmos. Sci.*, **28**, 181–189.

Chang, J. S., R. A. Brost, I. S. A. Isaken, S. Madronich, P. Middleton, W. R. Stockwell, and C. J. Walcek, 1987: A three-dimensional Eulerian acid deposition model: Physical concepts and formulation. *J. Geophys. Res.*, **92**, 14 681–14 700.

Deardorff, J., 1978: Efficient prediction of ground surface temperature and moisture, with inclusion of a layer of vegetation. *J. Geophys. Res.*, **83**, 1889–1903.

Detering, H. W., and D. Etling, 1985: Application of E–ϵ turbulence model to the atmospheric boundary layer. *Bound.-Layer Meteor.*, **33**, 113–133.

Gao, W., and M. L. Wesely, 1994: Numerical modeling of the turbulent fluxes of chemically reactive trace gases in the atmospheric boundary layer. *J. Appl. Meteor.*, **33**, 835–847.

Grell, G. A., J. Dudhia, and D. R. Stauffer, 1994: A description of the Fifth-Generation Penn State/NCAR Mesoscale Model (MM5). NCAR Tech. Note NCAR/TN 398 + STR, 138 pp. [Available from NCAR, MMM Division, P.O. Box 3000, Boulder, CO 80307.]

Hass, H., H. J. Jacobs, M. Memmesheimer, A. Ebel, and J. S. Chang, 1991: Simulation of a wet deposition case in Europe using the European Acid Deposition Model (EURAD). *Air Pollution Modeling and its Applications*, Vol. VIII, Plenum Press, 205–213.

Hicks, B. B., 1981: An analysis of Wangara micrometeorology: Surface stress, sensible heat, evaporation, and dewfall. NOAA Tech. Memo. ERL-104, Air Resources Laboratories, National Oceanic and Atmospheric Administration, Silver Spring, MD, 36 pp.

Holtslag, A. A. A., E. I. F. de Bruijn, and H.-L. Pan, 1990: A high resolution air mass transformation model for short-range weather forecasting. *Mon. Wea. Rev.*, **118**, 1561–1575.

Idso, S., R. Jackson, B. Kimball, and F. Nakayama, 1975: The dependence of bare soil albedo on soil water content. *J. Appl. Meteor.*, **14**, 109–113.

Jacquemin, B., and J. Noilhan, 1990: Sensitivity study and validation of land surface parameterization using the HAPEX-MOBILHY data set. *Bound.-Layer Meteor.*, **52**, 93–134.

Mahfouf, J. F., E. Richard, P. Mascart, E. C. Nickerson, and R. Rosset, 1987: A comparative study of various parameterizations of the planetary boundary layer in a numerical mesoscale model. *J. Climate Appl. Meteor.*, **26**, 1671–1695.

Mellor, C. L., and T. Yamada, 1974: A hierarchy of turbulence closure models for planetary boundary layers. *J. Atmos. Sci.*, **31**, 1791–1806.

Monin, A. S., and A. M. Yaglom, 1971: *Statistical Fluid Mechanics.* Vol. 1. The MIT Press, 468–504.

Noilhan, J., and S. Planton, 1989: A simple parameterization of land surface processes for meteorological models. *Mon. Wea. Rev.*, **117**, 536–549.

Pleim, J. E., and J. S. Chang, 1992: A non-local closure model for vertical mixing in the convective boundary layer. *Atmos. Environ.*, **26A**, 965–981.

——, and A. Xiu, 1995: Development and testing of a surface flux planetary boundary layer model with explicit soil moisture parameterization for applications in mesoscale models. *J. Appl. Meteor.*, **34**, 16–32.

Schumann, U., 1989: Large-eddy simulation of turbulent diffusion with chemical reactions in the convective boundary layer. *Atmos. Environ.*, **23**, 1–15.

Sellers, P. J., F. G. Hall, G. Asrar, D. E. Strebel, and R. E. Murphy, 1992: An overview of the First International Satellite Land Surface Climatology Project (ISLSCP) Field Experiment (FIFE). *J. Geophys. Res.*, **97**, 18 345–18 371.

Stull, R. B., and A. G. M. Driedonks, 1987: Applications of the transilient turbulence parameterization to atmospheric boundary layer simulations. *Bound.-Layer Meteor.*, **40**, 209–239.

Sun, W. Y., and W. R. Hsu, 1988: Numerical study of a cold air outbreak over the ocean. *J. Atmos. Sci.*, **45**, 1205–1227.